

The Oxide Scales Formed on a Dispersion-Strengthened Powder Metallurgical FeCrAl Alloy at 900 °C in O₂ and in O₂ + H₂O

K. Hellström · N. Israelsson · M. Halvarsson ·
S. Canovic · J.-E. Svensson · L.-G. Johansson

Received: 25 November 2014 / Revised: 28 January 2015 / Published online: 12 February 2015
© The Author(s) 2015. This article is published with open access at Springerlink.com

Abstract Early oxide scale growth on an oxide dispersion strengthened rapidly solidified powder FeCrAl material, Kanthal[®] APMT, was investigated at 900 °C in an O₂ + N₂ and an O₂ + H₂O + N₂ environment for up to 168 h. Gravimetry was used to follow oxide growth and the oxide scale was examined with XRD. Scale morphology was investigated in detail with SEM/EDX, TEM/EDX/CBED. The alloy rapidly formed a protective two-layered α -alumina scale containing oxide nodules. Between the top and bottom alumina layers there was a zone containing chromia-rich particles 5–20 nm in diameter, corresponding to the original sample surface. The alumina scale mainly grew inward after 1 h of oxidation. Alumina scale growth at 900 °C was initially somewhat faster in an O₂ + H₂O + N₂ environment than in an O₂ + N₂ environment.

Keywords FeCrAl · High-temperature oxidation · Water vapour

Introduction

FeCrAl alloys are widely used at high temperatures, e.g., as heating elements in furnaces and in many other industrial applications. The FeCrAl's have excellent ability to withstand oxidation and corrosion because of the formation of a slow-growing and adherent oxide scale consisting of α -Al₂O₃. Small amounts of so-called

K. Hellström · N. Israelsson (✉) · J.-E. Svensson · L.-G. Johansson
Department of Environmental Inorganic Chemistry, High Temperature Corrosion Centre,
Chalmers University of Technology, 412 96 Gothenburg, Sweden
e-mail: niklas.israelsson@chalmers.se

M. Halvarsson · S. Canovic
Department of Applied Physics, High Temperature Corrosion Centre, Chalmers University of
Technology, 412 96 Gothenburg, Sweden

reactive elements (RE) such as Y, Zr, Hf, Ce, and La are usually added to the alloys to improve the oxidation properties. It has been reported that the REs decrease the oxide growth rate, enhance selective oxidation and, especially, improve scale adherence [1–9]. Most of the research on the oxidation properties of FeCrAl alloys concerns temperatures $>1,000$ °C. This type of alloy is also used at lower temperatures. However, the amount of information on the oxidation behaviour of FeCrAl alloys at 900 °C and lower is limited, especially in an $O_2 + H_2O$ containing environment. While water vapour is present in many environments in which FeCrAl alloys are used, the literature concerning the influence of water vapour on FeCrAl oxidation is not extensive. Moreover, the literature is somewhat contradictory [10]. Some groups report lower oxidation rates in the presence of water vapour at about 1,000 °C [11, 12], whereas others report that the presence of water vapour accelerates oxidation initially at 900 °C [13] and at 1,300 °C [14]. It has also been reported that once a continuous Al_2O_3 scale has been formed, the oxidation is not significantly dependent on the water vapour content [15, 16]. As mentioned above, previous studies conducted by this group on the initial oxidation of the wrought FeCrAl alloy, Kanthal[®] AF, at 900 °C have shown that the oxide growth rate was initially somewhat faster in an $O_2 + H_2O$ environments than in a dry O_2 environment [13]. It has also been reported that the conversion of transient alumina to α -alumina was slower in the presence of H_2O [17]. The aim of this study is to examine the early stages of oxide scale growth on the dispersion-strengthened powder metallurgical FeCrAl alloy Kanthal[®] APMT at 900 °C in O_2 and in $O_2 + H_2O$. The results are compared with earlier studies of the wrought FeCrAl alloy Kanthal[®] AF.

Experimental Procedures

Material

The commercial dispersion strengthened powder metallurgical FeCrAl alloy Kanthal[®] APMT was investigated in the present study. Alloy APMT is a rapidly solidified powder (RSP) alloy which contains small refractory inclusions of oxides, carbides and nitrides homogeneously dispersed in the FeCrAl matrix. For further information, see Jönsson et al. [18, 19]. The nominal chemical composition of the alloy is given in Table 1. The material was supplied by Sandvik Heating Technology in the form of a 2 mm thick sheet, from which square samples (1.5×1.5 cm²) were prepared. These were ground and polished down to 1 μ m. The samples were cleaned in water, acetone and finally ethanol using ultrasonic

Table 1 The chemical nominal composition of Kanthal[®] APMT given in wt%

Element	Fe	Cr	Al	Mo	Mn	Si	C	RE
wt%	Bal.	21.0	5.0	3.0	≤ 0.4	≤ 0.7	≤ 0.08	Y, Zr, Hf, Ti

agitation. The samples were subsequently dried in flowing air and the weight was recorded on an analytical balance prior to oxidation.

Oxidation Exposure

Ex-situ

Alloy APMT, was exposed for 1, 24, 72 and 168 h at 900 °C in 5 % O₂ + 95 % N₂ and 5 % O₂ + 55 % N₂ + 40 % H₂O. The samples were set on an alumina holder positioned parallel to the direction of the gas flow in a horizontal tube furnace fitted with an alumina tube. A gas flow of 1,000 ml/min was used which correspond to 3.2 cm/s. Water vapour in the exposure atmosphere was generated by first passing the gas through heated water and then through a cooling system equipped with a thermostat set at the desired dew point. After exposure, the samples were allowed to cool in dry air. The samples were stored in a desiccator before analyses of the oxide scales.

In-situ

Oxidation experiments were carried out in a Setaram TGA thermo-balance. In the thermo-gravimetric analysis (TGA) the mass gain and the temperature of the sample were recorded continuously during the isothermal exposed at 900 °C for 72 h. The exposures were conducted in flowing gas (5 % O₂ + 95 % N₂ or 5 % O₂ + 40 % H₂O + 55 % N₂) having a flow rate of 15 ml/min which correspond to 0.3 cm/s. The thermo-balance was equipped with a double symmetrical furnace, where an Al₂O₃ sample with the same dimension as the FeCrAl sample was used as a reference in order to reduce the buoyancy effects. The specimen was heated at 99 °C/min to the isothermal exposure temperature (900 °C). The mass gain of each specimen was measured both before and after the exposure to verify the mass gain obtained during exposure in the TGA. At least two identical exposures were carried out at each exposure environment to establish reproducibility.

Grazing Incidence X-Ray Diffraction Analysis

The phase composition of the oxide scale was analysed with Grazing incidence X-ray diffraction (GI-XRD) using a Siemens D5000 powder diffractometer. Cu K α radiation was used. Measurements were performed between 20° < 2 θ < 60° (incidence angle = 0.5°, step size = 0.05°).

Electron Microscopy Analysis

The samples were examined with a FEI Quanta 200 FEG-ESEM equipped with an Oxford INCA EDX system. An accelerating voltage of 10–20 kV was used for imaging and EDX analysis. Before examining the cross-sections of the oxide scale with SEM/EDX, the samples were cast in Bakelite resin with carbon filler. Each

cross-section was then polished using increasingly finer grades of a diamond suspension, finishing with a $\frac{1}{4}$ μm silica suspension.

The transmission electron microscopy (TEM) and scanning transmission electron microscopy (STEM) parts of this study were conducted using a Philips CM 200 FEG TEM working at 200 kV and an FEI Titan 80/300 TEM/STEM equipped with an Oxford EDX detector and working at 300 kV. In order to identify the oxide phases present, convergent beam electron diffraction (CBED), in combination with STEM/EDX was used. TEM and STEM samples were prepared by a focus ion beam (FIB) in situ lift-out technique using an FEI Strata DB 235 M FIB–SEM.

Results

Alloy Microstructure

Figure 1a shows an SEM–BSE micrograph of alloy APMT before exposure. It may be noted that, in the as-received state, alloy APMT has a grain size of ≤ 1 to ~ 5 μm . Figure 1b shows a SEM micrograph of alloy APMT after 1 h exposure at 900 °C in dry O_2 , with a larger alloy grain size of about 10–20 μm . RE-rich particles appear as bright spots in Fig. 1 and the distribution seems not to have been affected by the alloy grain growth. The RE particles in alloy APMT ranged in typical size from <100 nm up to 0.5 μm . SEM/EDX analyses revealed that the larger RE particles in alloy APMT tended to be rich in Y, whereas the smaller ones were usually dominated by Hf and/or Zr. Small amounts of Ti were also present in the alloy. Ti is mainly associated with Hf and Zr.

Oxidation Kinetics

Figure 2a shows the ex situ mass gain curve for alloy APMT up to 168 h at 900 °C in O_2 and $\text{O}_2 + \text{H}_2\text{O}$ environments. As expected, the mass gains were quite small;

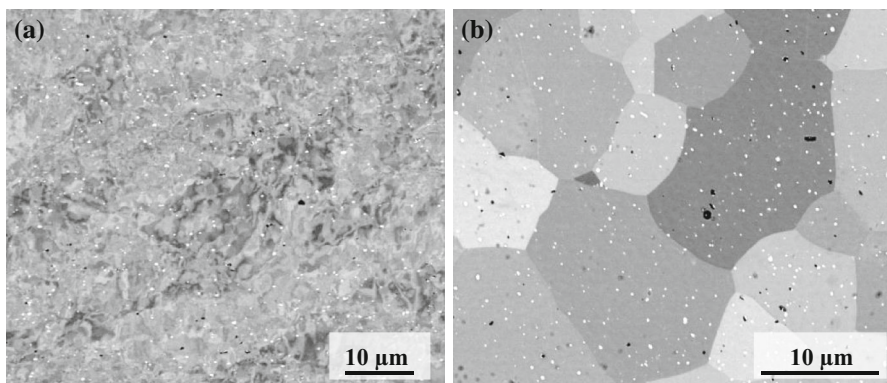


Fig. 1 SEM–BSE images of polished alloy APMT, showing the size and distribution of the reactive element particles and the grain size; **a** unexposed and **b** exposed for 1 h at 900 °C in dry O_2

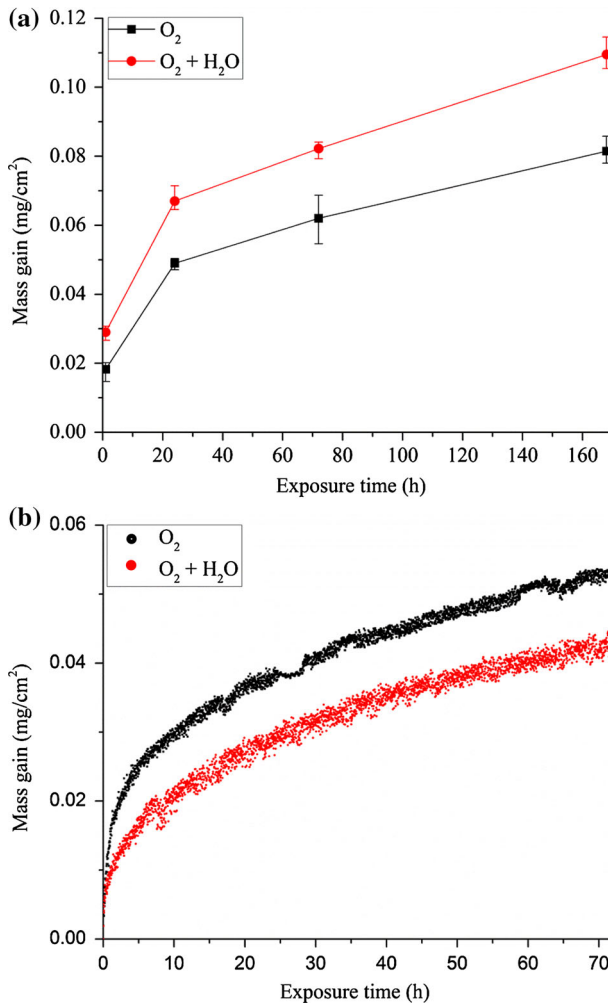


Fig. 2 Mass gain versus exposure time for alloy APMT exposed at 900 °C in O₂ and O₂ + H₂O. **a** ex-situ results from tube furnace exposures (1–168 h) and **b** in situ (TGA) exposures (up to 72 h)

about 0.08 mg/cm² in the O₂ environment and about 0.11 mg/cm² in the O₂ + H₂O environment after 168 h. This corresponds to an average scale thickness of 0.4–0.55 μm considering a 100 % dense α-alumina scale. Mass gain was relatively high during the first hour of exposure and then slowed down appreciably. The mass gain was more or less linear between 24 and 168 h. Mass gain was significantly greater in the presence of H₂O; the effect was the most marked the first 24 h. Figure 2b shows the corresponding in situ mass gain curves at 900 °C up to 72 h. When comparing the in situ and ex situ mass gain curves it may be noted that the in situ mass gain measurements only started after 900 °C was reached. This means that the mass gain during the 9-min heat-up period was not recorded. This implies

that the mass gains recorded in situ can be expected to be slightly lower than the ex situ mass gains. It may be noted that the in situ mass gain was somewhat higher in an O_2 than in an $O_2 + H_2O$ environment. This apparent contradiction to the ex situ results is also attributed to the differences mentioned above. There were no signs of spallation of the oxide during or after exposure.

Phase Composition of the Scales

Figure 3 shows XRD patterns acquired after 1 and 168 h in an $O_2 + N_2$ environment. The diffraction patterns recorded after exposure in an $O_2 + H_2O$ environment were essentially the same (not shown). The only oxide identified was $\alpha\text{-Al}_2\text{O}_3$, irrespective of environment and exposure time. As expected, the intensity of the $\alpha\text{-Al}_2\text{O}_3$ peaks increased with exposure time, as the oxide grew thicker.

Top-View SEM/EDX

Figure 4 shows top-view SEM images of the oxidized samples. As expected, the morphology of the scale surface became coarser with longer exposure time. The effect of water vapour on surface morphology was only seen initially, the oxide nodules formed after 1 h in the O_2 environment were about twice the size of the nodules formed in the absence of water.

Cross Section SEM/EDX

Figure 5 shows scale cross-sections after 1, 24 and 168 h in O_2 and $O_2 + H_2O$ environments. In accordance with the ex situ gravimetric data (Fig. 2a), the alumina scale formed in $O_2 + H_2O$ environment was somewhat thicker than in the O_2 environment. The alumina scale consisted of two layers and the microstructure was

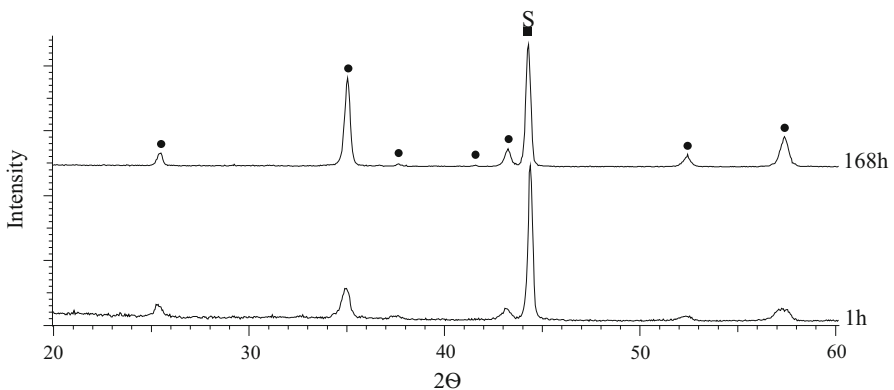


Fig. 3 XRD patterns of alloy APMT after exposure at 900 °C for 1 and 168 h in O_2 . Peak positions are given for $\alpha\text{-Al}_2\text{O}_3$ (filled circles) and for the alloy substrate (S). The peak intensities are normalised with respect to the substrate peak

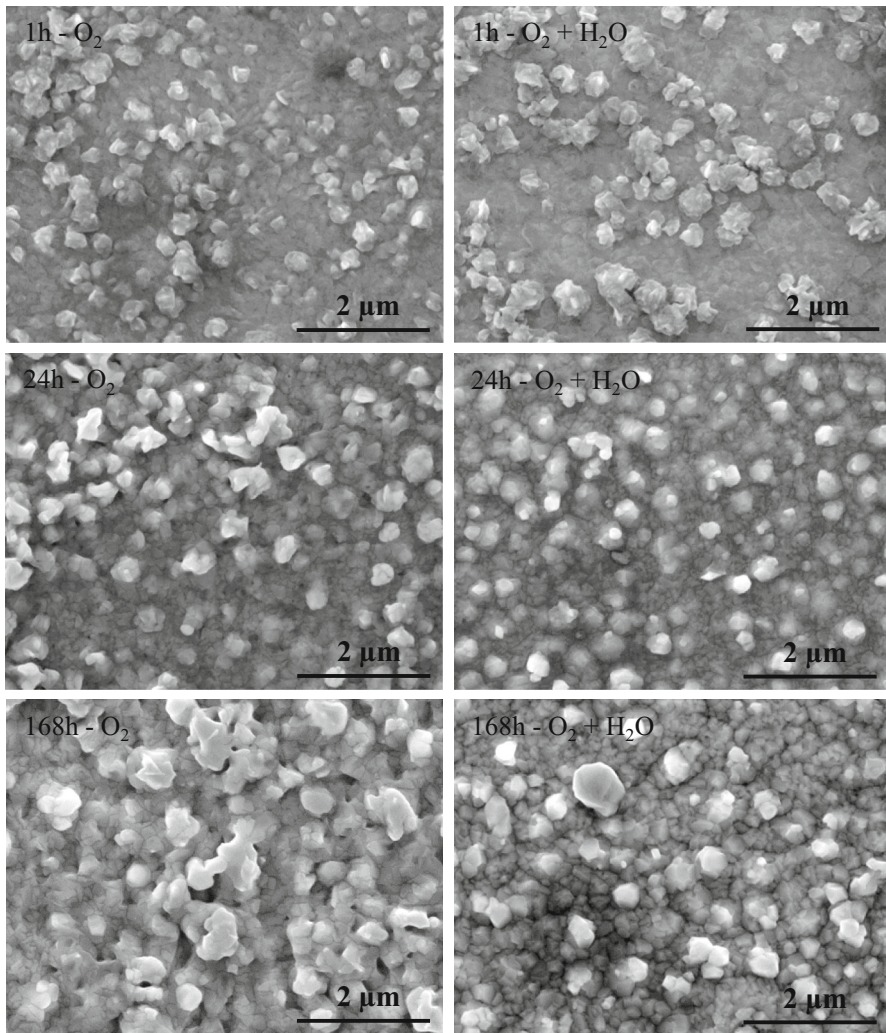


Fig. 4 Top-view SEM–SE images of alloy APMT after 1, 24 and 168 h exposure in O_2 and $O_2 + H_2O$ at 900 °C

not strongly dependent on the presence of water vapour. The micrographs show a relatively dark top layer and a brighter bottom layer that are separated by a straight interface. The brightness of the bottom layer is due to charging of alumina during imaging. Because the top layer was more conductive than the bottom layer, an image that clearly separates the two layers could be achieved by imaging before the top layer started to charge. The top layer did not grow considerably with exposure time, i.e. between 1 and 168 h, scale growth occurred mainly in the bottom layer. The thickness of the alumina scale showed substantial variations over the sample surface (Table 2). However, the estimated average oxide thicknesses showed fair agreement with the ex situ mass gains, i.e. increasing from about 0.1 μm after 1 h to

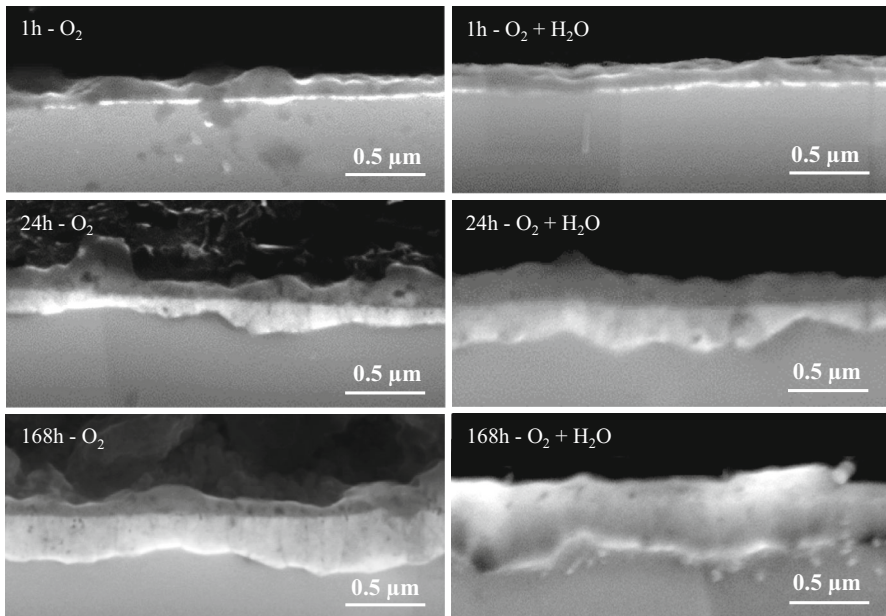


Fig. 5 SEM–SE images of cross-sections of the oxide scale formed on alloy APMT after 1, 24 and 168 h exposure in O_2 and $O_2 + H_2O$ at 900 °C

Table 2 Thickness of the alumina scale (base oxide) measured in cross-sections using SEM and TEM on alloy APMT exposed at 900 °C in O_2 and $O_2 + H_2O$ for 1, 24 and 168 h

Exposure time (h)	O_2 (μm)	$O_2 + H_2O$ (μm)
1	0.07–0.22	0.08–0.32
24	0.25–0.44	0.26–0.52
168	0.41–0.66	0.41–0.57

0.5 μm after 168 h. Figure 6 shows an SEM micrograph of a scale cross-section after 168 h in the O_2 environment. RE-rich particles of different sizes were present in the alloy substrate and in the bottom scale layer. The larger RE-rich particles were rich in yttrium.

TEM Cross Sections

To obtain more detailed information about the scale microstructure during initial oxidation, TEM samples were prepared after 1 h oxidation in O_2 and $O_2 + H_2O$ environments (Fig. 7). In both environments, oxidation produced an oxide scale consisting of two alumina layers. The top and bottom alumina layers were separated by a somewhat darker line. While the bottom alumina layer was rather even with a thickness of about 20 nm, the top alumina layer had two distinctive appearances. First, there was an “even top layer”, featuring an even thickness and consisting of

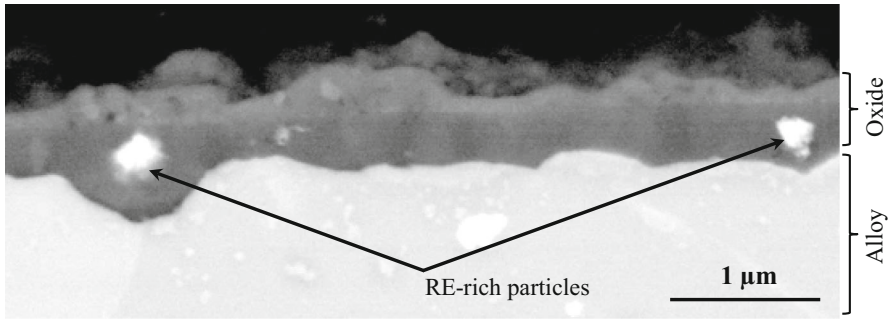


Fig. 6 SEM–BSE micrograph of a cross-section of the oxide scale formed on alloy APMT after 168 h exposure in O_2 at 900 °C, showing a two-layered oxide scale with two entrapped RE-rich particles

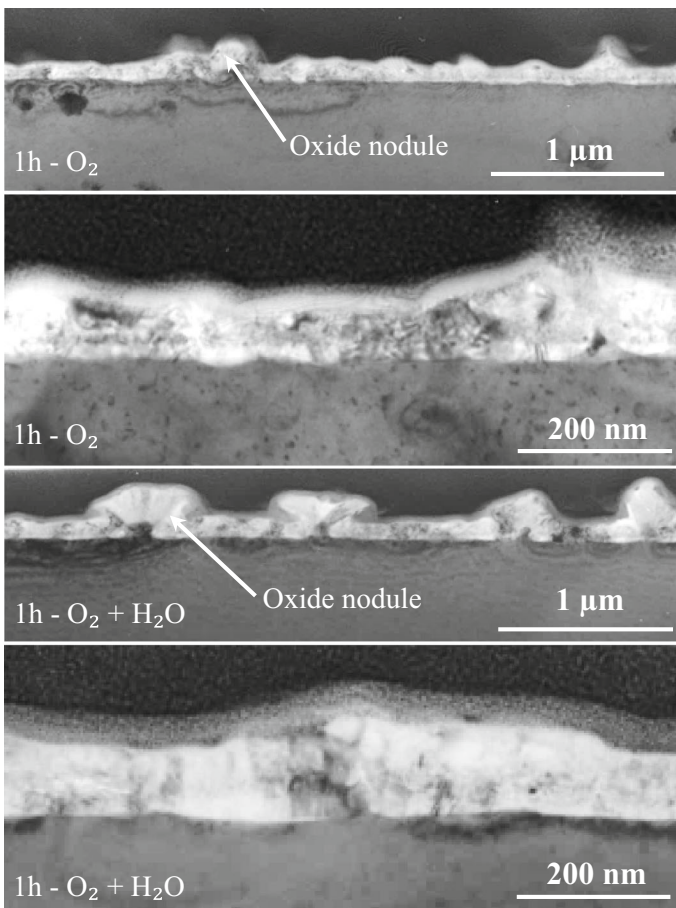


Fig. 7 TEM–BF images of the cross-sections of the oxide scale formed on alloy APMT after 1 h exposure in O_2 and $O_2 + H_2O$ at 900 °C

equi-axed grains. The “even top layer” was about 50 nm thick in O_2 and about 75 nm in an $O_2 + H_2O$ environment. The remaining part of the top alumina layer consisted of “oxide nodules” with up to four times the thickness of the “even top layer” and consisting of elongated/columnar grains. The “oxide nodules” are assumed to correspond to the oxide nodules observed in the top-view image (c.f. Figure 4). In line with the top-view imaging, the oxide nodules were larger in the $O_2 + H_2O$ than in the O_2 environment.

Figure 8 shows a cross-section STEM image after one hour exposure in the O_2 environment. The EDX point analyses, marked in Fig. 8, revealed that the dark line separating the top and bottom alumina layers in Fig. 7 was enriched in Cr. The Cr-rich line appears with bright contrast in Fig. 8 because Cr is heavier than Al. Figure 9 shows an EDX line-scan across the scale acquired from the same sample. The Cr-enrichment can clearly be seen, reaching a maximum of 30 at% (cationic). In addition, the line-scan showed that while the bottom layer of the scale was essentially pure aluminium oxide, the top alumina layer contained about 10 at% Fe (cationic). Figure 10 shows a corresponding line-scan after 1 h exposure in an $O_2 + H_2O$ environment. In line with the cross-sections shown in Fig. 7, the top alumina layer was somewhat thicker here than in the O_2 environment. The elemental composition of the scale was similar to that observed after oxidation in the O_2 environment. The top alumina layer in Fig. 10 featured higher concentrations of iron than in the corresponding exposure in the dry environment. However, the Fe content in the top alumina layer varied laterally in the scale and is reflected in the varying contrast in the STEM-HAADF micrographs; brighter regions being more Fe-rich, see Figs. 9 and 10.

Figure 11 shows a STEM-HAADF image of a scale cross-section from the sample exposed for 1 h in the O_2 environment, which exhibits the two-layered alumina scale with the Cr-enriched regions in between. The latter consisted of bright rounded Cr-rich particles (analysed with EDX) in the size range <5–20 nm. The darker area between the particles corresponds to alumina. Thus, it can be concluded that the Cr-enriched “line” is actually made up of <5–20 nm diameter Cr-rich oxide

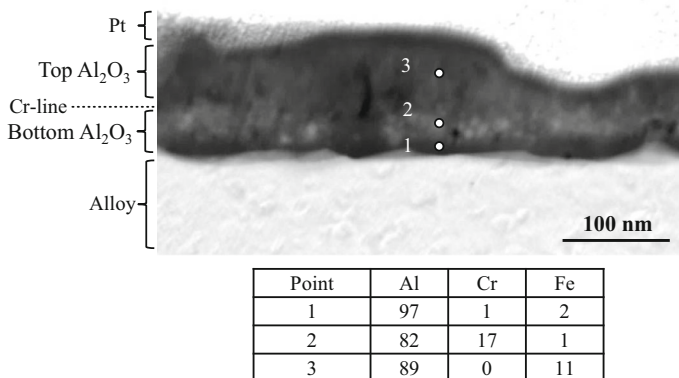


Fig. 8 STEM-HAADF image of the cross-section and EDX point analyses (cation at%) of the oxide scale formed on alloy APMT after 1 h exposure in O_2 at 900 °C

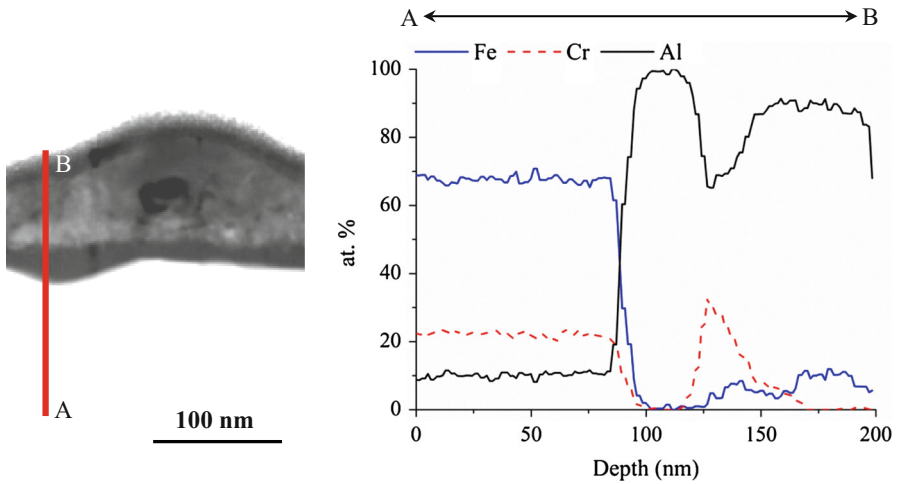


Fig. 9 STEM-HAADF image and EDX line-scan through the formed oxide scale on alloy APMT after 1 h exposure in O_2 at 900 °C

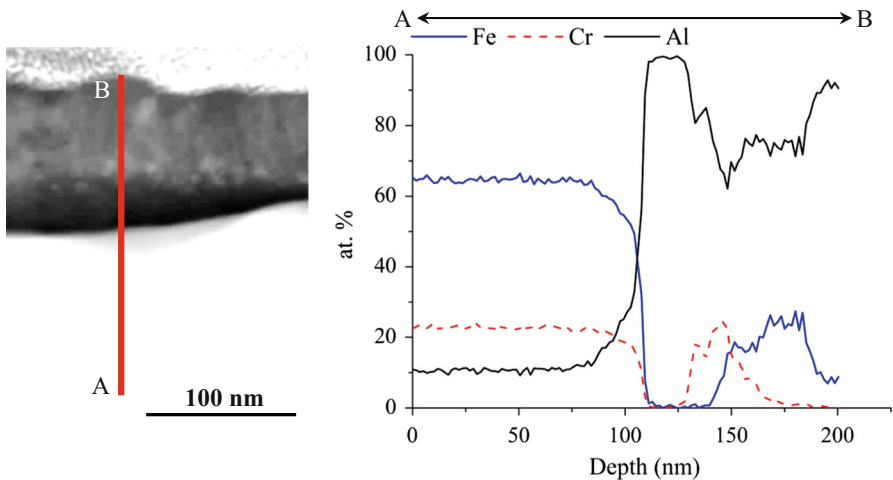


Fig. 10 STEM-HAADF image and EDX line-scan through the formed oxide scale on alloy APMT after 1 h exposure in $O_2 + H_2O$ at 900 °C

particles immersed in an alumina matrix. Evidence of porosity (very dark contrast) was detected outside the Cr-enriched line. Moreover, relatively large regions with a brighter contrast could be observed outside of the Cr-rich line, in the top part of the scale. The latter are tentatively attributed to enrichments of Fe. The phase composition of the top and bottom alumina layers was determined using CBED shown in Figs. 12 and 13. Patterns were acquired from both the top and bottom alumina layers after 1 h of exposure in both environments. All diffraction patterns could be indexed as α - Al_2O_3 .

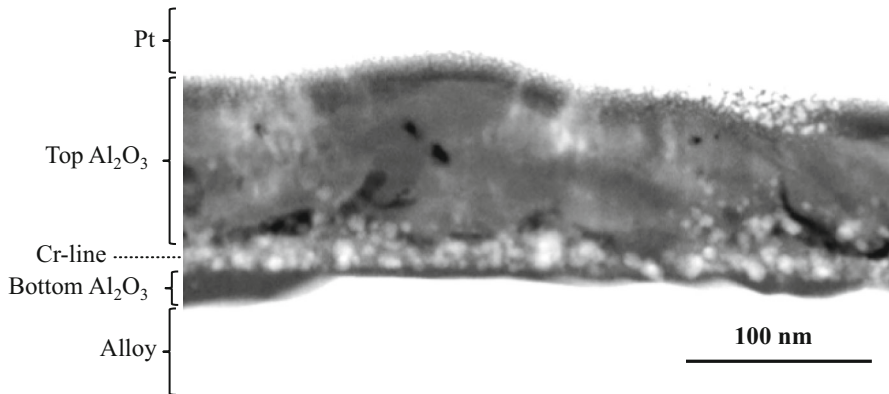


Fig. 11 STEM-HAADF image of a cross-section of the formed oxide scale after 1 h exposure in O₂ at 900 °C

Figure 14 is a STEM-HAADF image of a scale cross-section prepared after 1 h exposure in the O₂ environment. The image shows the oxide scale with one larger oxide nodule at the centre. With the strong image contrast in Fig. 14 it appears that there is a metal protrusion sticking up from the alloy into the oxide nodule. To further investigate the oxide nodule and neighbouring regions in the alloy and oxide scale, STEM-EDX elemental mapping was performed in the rectangular area indicated in Fig. 15. Using slightly less image contrast, as in Fig. 15 (compared to Fig. 14) the protrusion appears with a contrast in between that of the metal and the oxide scale. This can either be due to another phase present in the protrusion or to a geometrical overlap between a metal protrusion and the oxide scale in the thin foil specimen. The oxide nodule and the top and bottom oxide layers on each side of the nodule consisted of almost pure alumina, the Fe and Cr levels were <1 at%. The bright line in the figure, or rather the row of bright particles, separating the inner and outer oxide layers, is Cr-rich, the composition was 35 at% Al, 5 at% Cr and 60 at% O, the Fe level still being <1 at%. From the EDX maps and the HAADF image it was clear that the Cr-rich band did not bend around the protrusion. The oxygen map shows that the protrusion region exhibits a relatively low oxygen level. Quantitative analysis of the EDX maps showed that this region contained about 45 at% O. The low oxygen signal is likely due to an overlap of a metallic protrusion and oxide, i.e. the alloy and alumina are superimposed in the analysis. If the Al and O content from the overlapping oxide part is subtracted from the analysis, the remaining composition (the metal part) roughly matches that of the alloy. In other words, below the central part of the nodule there is a metallic protrusion which is connected to the alloy substrate and partly surrounded by the alumina scale.

Discussion

The ex situ mass gains in this study are close to those reported in other studies of FeCrAl alloys with RE additions [20–22], and are similar to the values reported for

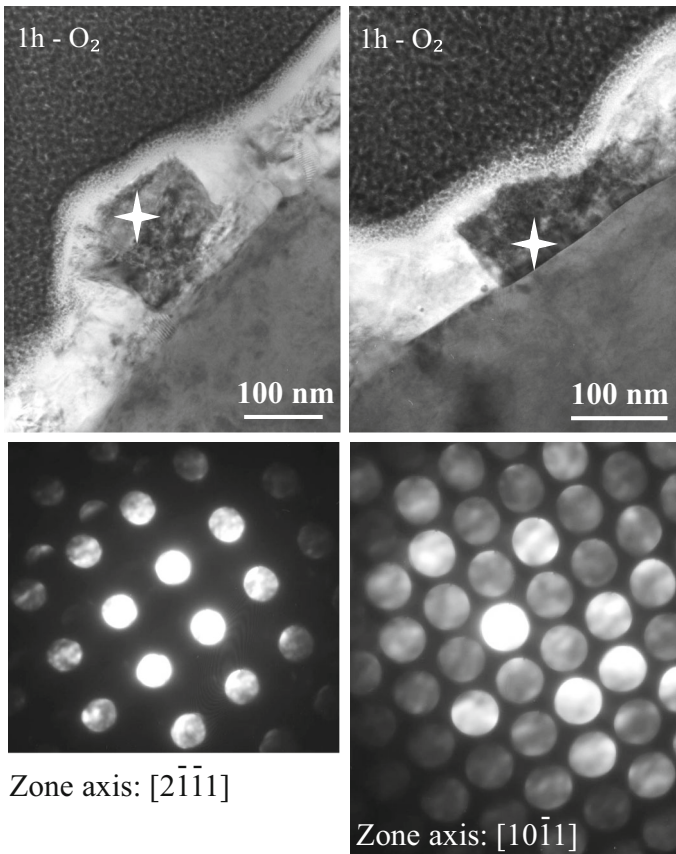


Fig. 12 TEM-BF images of cross-section and CBED patterns from the oxide scale formed on alloy APMT after 1 h exposure in O₂ at 900 °C. The stars indicate where the diffraction patterns were obtained. The diffraction pattern from the *top* and *bottom* layer could both be indexed as α -Al₂O₃

the wrought FeCrAl alloy Kanthal[®] AF in O₂ and O₂ + H₂O environments [13, 23]. The ex situ mass gains and scale thicknesses obtained with SEM and TEM all indicate that the rate of scale growth is somewhat higher in an O₂ + H₂O than in an O₂ environment. The mass gain curves in Fig. 2a imply that the presence of water vapour primarily affects the early stages of oxidation. This is in line with Fig. 4, which shows that after 1 h the oxide nodules are larger in the presence of H₂O. This is also supported by the TEM images of the cross-sections in Fig. 7 which show that the oxide nodules are more pronounced in the presence of water vapour. The influence of water vapour on early oxide growth is consistent with the initial oxidation-accelerating effect of water vapour in O₂-containing environment, recently reported for the same alloy at 1,100 °C [24]. The somewhat contradictory in situ results, showing a slightly smaller mass gain in the presence of H₂O, is suggested to be explained by the mass gain that occurs during sample heat-up and which was not recorded in the in situ measurements (see “Results” section).

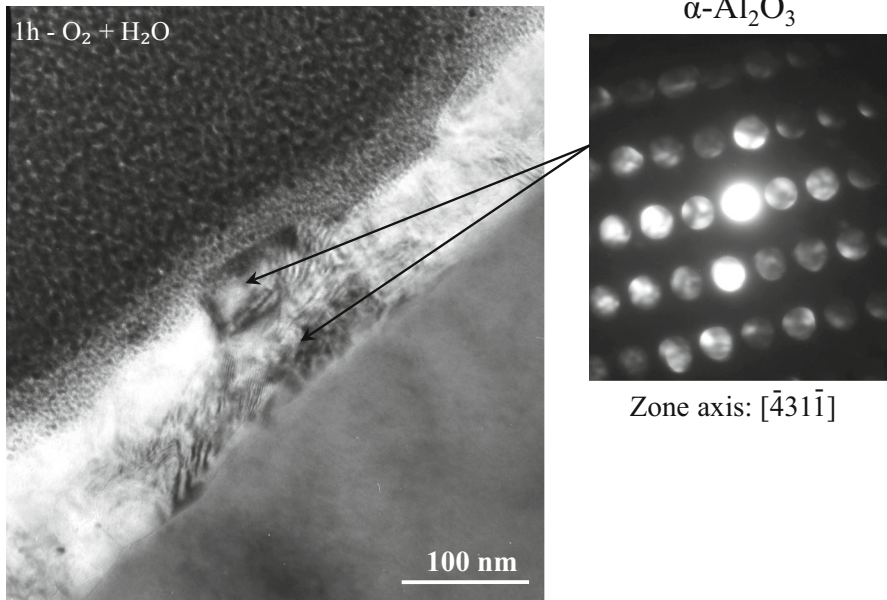


Fig. 13 TEM-BF image of a cross-section and CBED pattern from the oxide scale formed on alloy APMT after 1 h exposure in O₂ + H₂O at 900 °C. The diffraction pattern from the *top* and *bottom* layer could both be indexed as α-Al₂O₃

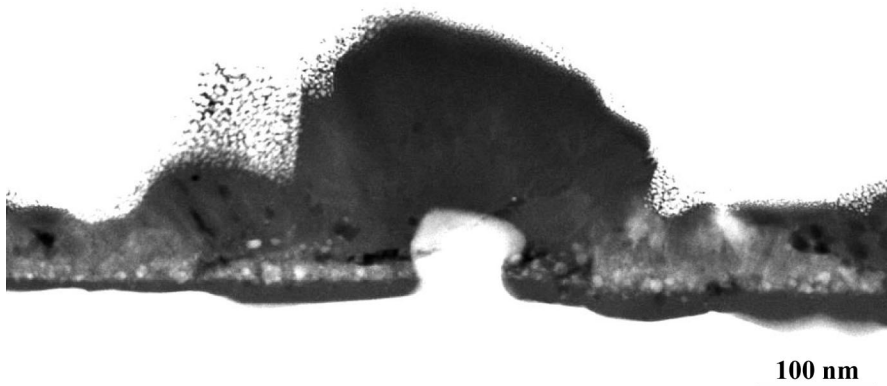


Fig. 14 STEM-HAADF image of a cross-section of the oxide scale formed on alloy APMT after 1 h exposure in O₂ at 900 °C

After 1 h of exposure at 900 °C, the alloy had already formed a continuous and protective two-layered α-alumina scale in which the top and bottom layers were separated by a region containing chromia-rich particles, (see Figs. 8, 9, 10, 11). In addition, iron was unevenly distributed in the top alumina layer (Fig. 10). Similar results were obtained with TEM and SIMS analyses for the sample exposed for 72 h

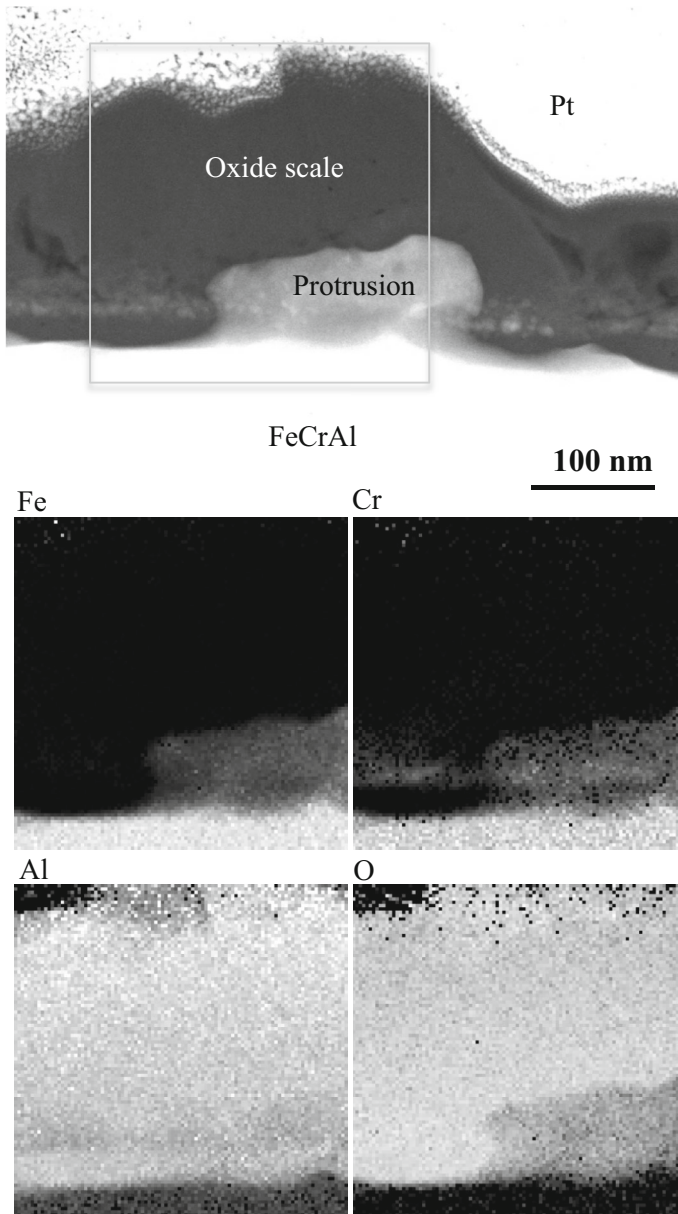


Fig. 15 STEM-HAADF image of cross-section and EDX elemental maps of the of the oxide scale formed on alloy APMT after 1 h exposure in O_2 at 900 °C

in dry O_2 , published elsewhere [24]. The formation of a two-layered alumina scale containing a Cr-rich band has been reported earlier for FeCrAl alloys [13, 25–28]. In accordance with Götlind et al. and Liu et al. [13, 17], who investigated the oxidation

properties of a wrought FeCrAl alloy at 900 °C, it is assumed that both iron and chromium entered the scale during transient oxidation, i.e. during sample heat-up and in the first few minutes at temperature. Also in line with Götlind et al. and Liu et al. [13, 17], it is proposed that the bottom alumina layer has grown by inward diffusion of oxygen ions, that the top alumina layer has grown by outward diffusion of cations and that, consequently, the chromia-enriched zone corresponds to the original sample surface. The observation that chromia formed discrete particles rather than being dispersed in the alumina matrix, is suggested to reflect the very limited solubility of chromia in α -alumina at 900 °C [29]. Previous investigations on the melt-processed alloy Kanthal[®] AF [13, 17] did not detect discrete chromia-rich particles due to limitations in the analysis. In contrast to Cr, Fe was mainly detected in the top alumina layer. The tendency for Fe to be distributed outside the Cr-enriched line has been reported previously by Liu et al. [17]. In line with that paper, it is assumed that iron (Fe^{2+}) has a higher mobility in the alumina scale than chromium (Cr^{3+}).

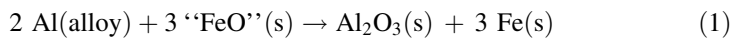
This study shows that the top alumina layer does not grow significantly after exposure times >1 h (see Fig. 5). Thus, further scale growth mainly occurred in the bottom alumina layer (Fig. 5). The dominance of inward growth is in line with many reports in the literature on the suppression of outward growth in alumina scales by Y- and other RE-ions that accumulate at the Al_2O_3 grain boundaries [2, 30–32]. It may be noted that under the same conditions (polished surface, 900 °C, O_2 and $\text{O}_2 + \text{H}_2\text{O}$ environment), the melt-processed FeCrAl alloy Kanthal[®] AF exhibited significant and continuous outward scale growth [23]. Consequently, outward scale growth appears to be more efficiently suppressed on alloy APMT than on alloy AF. It is suggested that the tendency for outward scale growth is related to differences in the REs present in the two alloys. In other words, while the REs are added in the form of oxide dispersion to Kanthal[®] APMT, they are added to alloy AF in elemental form. Moreover, alloy APMT contains Hf while alloy AF does not.

Several researchers have reported that FeCrAl alloys forms transient metastable aluminas at 900 °C, showing needle or platelet shapes, see e.g. Kadiri et al. [33]. However no transient forms of alumina were detected in this study. Thus, the oxide scale consisted of α - Al_2O_3 after all exposure times, as shown by GI-XRD and CBED (see Figs. 3, 12, 13). In other words, if metastable alumina formed during the initial oxidation, it had already transformed into α - Al_2O_3 after 1 h at 900 °C. Interestingly, the outer oxide layer of the melt-processed FeCrAl alloy Kanthal[®] AF was reported to contain γ - Al_2O_3 after up to 168 h at 900 °C in O_2 and $\text{O}_2 + \text{H}_2\text{O}$ environments [13, 17, 27]. This implies that the formation of α - Al_2O_3 is faster on Kanthal[®] APMT than on Kanthal[®] AF. According to Pint et al. [31], the presence of an oxide dispersion in the alloy may create nucleation sites for α -alumina. Accordingly, it is suggested that the prevalence of α -alumina over the transient aluminas in the dispersion-strengthened powder metallurgical FeCrAl alloy is due to α -alumina, present in the alloy matrix, providing nucleation sites for α -alumina in the external scale.

In order to produce a clean and smooth surface in a reproducible way, facilitating the investigation of the thin oxide scales formed, the sample surface was polished down to 1 μm with diamond paste before exposure. It may be questioned how the

present results relate to materials used in industrial applications with a much rougher surface. El Kadiri et al. [5] showed that the formation of oxide nodules was favoured at polishing marks on FeCrAl alloys exposed at 900 °C, suggesting that rough surfaces oxidizes faster initially. However, the main scale features appears to be independent of surface roughness. Thus, similar to the present work, K.A. Unocic et al. [11] showed that a two layered alumina scale with equiaxed grains in the top layer and columnar grains in the bottom layer grew on a 600 grit FeCrAl surface in an similar environment. Also, Chevalier et al. [34] reported the formation of similar oxide scales on a FeCrAl foil without any grinding and polishing before exposure.

In addition to the layered oxide described above, the scale observed after 1 h also featured oxide nodules/metal protrusions, (see Figs. 4, 7, 14, 15). Beneath the oxide nodules and embedded in the alumina scale, metallic protrusion in the size range 50–100 nm were observed that were connected to the alloy substrate. The oxide nodules were not associated with RE particles. While oxide nodules have been observed previously, the authors are not aware of reports of metallic protrusions at the base of oxide nodules. Somewhat similar features have been reported recently by Hall et al. [35] who worked with the oxidation properties of an austenitic FeNiCrAl alloy. In that study, metallic particles and protrusions in the size range <0.1–0.4 μm were observed in the oxide scale after 10 min at 900 °C. It was argued that the metallic scale inclusions had formed by a redox reaction between the oxides of Ni and Fe oxide (in the transient oxide) and the metal substrate, resulting in the formation of metallic Fe and Ni. It is suggested that the metallic protrusions observed in the present study have formed in a similar way, through reduction of Fe oxide (and perhaps Cr oxide) by Al in the metal substrate:



(“FeO” is taken to represent the poorly defined iron oxide formed in the initial, transient stages of oxidation)

It may be noted that direct contact between FeO in the oxide layer and the alloy substrate is a prerequisite for Reaction (1) to occur. This implies that the reaction ceases once the inward-growing alumina layer is established. If Reaction (1) is responsible for the metallic protrusions, they would initially consist of pure Fe. However, the EDX analysis (see above) indicated that the composition of the protrusions was similar to that of the alloy after 1 h. This apparent contradiction can be explained by the high temperature and the small size of the protrusions, allowing Al and Cr to diffuse from the alloy into the protrusions within 1 h. This is supported by the STEM/EDX line-scans in Figs. 9 and 10, which show no depletion of the alloying elements underneath the alumina scale after 1 h at 900 °C. It has already been noted that the top part of the layered alumina scale contained appreciable amounts of iron (Figs. 8, 9, 10). In contrast, the iron content in the oxide nodule and close to it was <1 at%, according to the STEM-EDX analyses. It is suggested that the low iron content in the oxide nodule is explained by Reaction (1), in which iron oxide in the transient oxide is converted to metallic iron in the protrusion.

Because it is essential that a protective external oxide layer is rapidly established, it is important to understand the early oxidation behaviour of high temperature

alloys. One of the main contributions of the present study is the observation of metallic protrusions forming during early oxidation. The formation of the oxide nodules in connection to the metallic protrusions appears to delay the formation of the inward growing alumina layer which likely compromises the initial protective behaviour of the alumina scale. Other contributions to the understanding of early oxidation include a detailed morphology of the two-layered alumina scale and the role of oxide grains in the alloy matrix in promoting the formation of an α -alumina protective scale.

Conclusions

- The alloy rapidly formed a protective two-layered α -alumina scale containing oxide nodules. Between the *top* and *bottom* alumina layers there was a band containing 5–20 nm diameter chromia-rich particles.
- It is proposed that the bottom alumina layer had grown by means of the inward diffusion of oxygen ions, that the top layer had grown by the means of the outward diffusion of cations and that the chromia-enriched band corresponds to the original sample surface.
- Oxide nodules formed on top of 50–100 nm size metallic protrusions connected to the substrate. It is suggested that the metal protrusions formed by the reduction of iron oxide in the transient oxide by Al in the alloy.
- Unlike chromium, iron was unevenly distributed in the top scale layer.
- After >1 h, the alumina scale mainly grew inward.
- α -Al₂O₃ was the only aluminium oxide detected. The absence of metastable aluminas is tentatively attributed to the presence of α -Al₂O₃ grains in the alloy matrix which help nucleate the α -alumina in the scale.
- Oxide growth was initially faster in O₂ + H₂O environment than in dry O₂. During later stages, the rate of oxidation in dry and wet O₂ was the same.

Acknowledgments This research was conducted at the Swedish High Temperature Corrosion Centre (HTC) at Chalmers University of Technology.

Open Access This article is distributed under the terms of the Creative Commons Attribution License which permits any use, distribution, and reproduction in any medium, provided the original author(s) and the source are credited.

References

1. W. J. Quadakkers, H. Holzbrecher, K. G. Briefs and H. Beske, *Oxidation of Metals* **32**, 67 (1989).
2. B. A. Pint, A. J. Garrett-Reed and L. W. Hobbs, *Materials at High Temperatures* **13**, 3 (1995).
3. W. J. Quadakkers, A. Elschner, W. Speier and H. Nickel, *Applied Surface Science* **52**, 271 (1991).
4. J. R. Blachère, E. Schumann, G. H. Meier and F. S. Pettit, *Scripta Materialia* **49**, 909 (2003).
5. H. El Kadiri, R. Molins, Y. Bienvenu and M. F. Horstemeyer, *Oxidation of Metals* **64**, 63 (2005).

6. M. Le Gall, A. M. Huntz, B. Lesage, C. Monty and J. Bernardini, *Journal of Materials Science* **30**, 201 (1995).
7. J. A. Nychka and D. R. Clarke, *Oxidation of Metals* **63**, 325 (2005).
8. D. P. Whittle and J. Stringer, *Philosophical Transactions of the Royal Society A* **295**, 309 (1980).
9. P. Y. Hou, *Materials Science Forum* **696**, 39 (2011).
10. S. R. J. Saunders, M. Monteiro and F. Rizzo, *Progress in Materials Science* **53**, 775 (2008).
11. K. A. Unocic, E. Essuman, S. Dryepondt and B. A. Pint, *Materials at High Temperatures* **29**, 171 (2012).
12. H. Buscail, S. Heinze, P. Dufour and J. P. Larpin, *Oxidation of Metals* **47**, 445 (1997).
13. H. Götlind, F. Liu, J.-E. Svensson, M. Halvarsson and L.-G. Johansson, *Oxidation of Metals* **67**, 251 (2007).
14. H. Al-Badairy and G. J. Tatlock, *Materials at High temperatures* **17**, 133 (2000).
15. I. Kvernes, M. Oliveira and P. Kofstad, *Corrosion Science* **17**, 237 (1977).
16. H. Al-Badairy and G. J. Tatlock, *Materials at High Temperatures* **18**, 101 (2001).
17. F. Liu, H. Götlind, J.-E. Svensson, L.-G. Johansson and M. Halvarsson, *Corrosion Science* **50**, 2272 (2008).
18. B. Jönsson, Q. Lu, D. Chandrasekaran, R. Berglund and F. Rave, *Oxidation of Metals* **79**, 29 (2013).
19. B. Jönsson, R. Berglund, J. Magnusson, P. Henning and M. Hättestrand, *Materials Science Forum* **461–464**, 455 (2004).
20. J. Jedlinski, B. Cohat and G. Borchardt, *High Temperature Materials and Processes* **13**, 241 (1994).
21. J. L. González-Carrasco, M. C. García-Alonso, M. A. Montealegre, M. L. Escudero and J. Chao, *Oxidation of Metals* **55**, 209 (2001).
22. J. L. González-Carrasco, M. C. García-Alonso, M. L. Escudero and J. Chao, *Oxidation of Metals* **53**, 77 (2000).
23. F. Liu, H. Gotlind, J. E. Svensson, L. G. Johansson and M. Halvarsson, *Oxidation of Metals* **74**, 11 (2010).
24. J. Engkvist, S. Canovic, K. Hellström, A. Järnäs, J.-E. Svensson, L.-G. Johansson, M. Olsson and M. Halvarsson, *Oxidation of Metals* **73**, 233 (2010).
25. L. Marechal, B. Lesage, A. M. Huntz and R. Molins, *Oxidation of Metals* **60**, 1 (2003).
26. M. A. Montealegre, G. Strehl, J. L. González-Carrasco and G. Borchardt, *Intermetallics* **13**, 896 (2005).
27. F. Liu, H. Josefsson, J. E. Svensson, L. G. Johansson and M. Halvarsson, *Materials at High Temperatures* **22**, 521 (2005).
28. B. A. Pint, A. J. Garratt-Reed and L. W. Hobbs, *Oxidation of Metals* **56**, 119 (2001).
29. T. M. Besmann, N. S. Kulkarni and K. E. Spear, *Journal of the American Ceramic Society* **89**, 638 (2006).
30. K. Przybylski, A. J. Garratt-Reed, B. A. Pint, E. P. Katz and G. J. Yurek, *Journal of the Electrochemical Society* **134**, 3207 (1987).
31. B. A. Pint, *Oxidation of Metals* **45**, 1 (1996).
32. B. A. Pint, J. R. Martin and L. W. Hobbs, *Oxidation of Metals* **39**, 167 (1993).
33. H. E. Kadiri, R. Molins, Y. Bienvenu and M. F. Horstemeyer, *Oxidation of Metals* **64**, 63 (2005).
34. S. Chevalier, K. Przybylski, G. Borchardt and J. P. Larpin, *High Temperature Corrosion and Protection of Materials* 6, Part 1 and 2, Proceedings **461–464**, 53 (2004).
35. J. Hall, K. Hellström, J. E. Svensson, M. Norell, M. Lundberg, T. Helander and L. G. Johansson, *Oxidation of Metals* **82**, 225 (2014).